The merging cluster Abell 1758 revisited: multi-wavelength observations and numerical simulations

F. Durret, T. F. Laganá, M. Haider

A&A 529, A38 (2011)
DOI: 10.1051/0004-6361/201015978

Astronomy & Astrophysics

The merging cluster Abell 1758 revisited: multi-wavelength observations and numerical simulations⋆

F. Durret[1,2], T. F. Laganá[3], and M. Haider[4]

[1] UPMC Université Paris 06, UMR 7095, Institut d'Astrophysique de Paris, 75014 Paris, France
e-mail: durret@iap.fr
[2] CNRS, UMR 7095, Institut d'Astrophysique de Paris, 75014 Paris, France
[3] IAG, USP, R. do Matão 1226, 05508-090 São Paulo/SP, Brazil
[4] Inst. of Astro and Particle Physics, University of Innsbruck, 6020 Innsbruck, Austria

Received 22 October 2010 / Accepted 4 February 2011

ABSTRACT

Context. Cluster properties can be more distinctly studied in pairs of clusters, where we expect the effects of interactions to be strong.
Aims. We here discuss the properties of the double cluster Abell 1758 at a redshift $z \sim 0.279$. These clusters show strong evidence for merging.
Methods. We analyse the optical properties of the North and South cluster of Abell 1758 based on deep imaging obtained with the Canada-France-Hawaii Telescope (CFHT) archive Megaprime/Megacam camera in the g' and r' bands, covering a total region of about 1.05×1.16 deg^2, or 16.1×17.6 Mpc^2. Our X-ray analysis is based on archive *XMM-Newton* images. Numerical simulations were performed using an N-body algorithm to treat the dark-matter component, a semi-analytical galaxy-formation model for the evolution of the galaxies and a grid-based hydrodynamic code with a parts per million (PPM) scheme for the dynamics of the intra-cluster medium. We computed galaxy luminosity functions (GLFs) and 2D temperature and metallicity maps of the X-ray gas, which we then compared to the results of our numerical simulations.
Results. The GLFs of Abell 1758 North are well fit by Schechter functions in the g' and r' bands, but with a small excess of bright galaxies, particularly in the r' band; their faint-end slopes are similar in both bands. In contrast, the GLFs of Abell 1758 South are not well fit by Schechter functions: excesses of bright galaxies are seen in both bands; the faint-end of the GLF is not very well defined in g'. The GLF computed from our numerical simulations assuming a halo mass-luminosity relation agrees with those derived from the observations. From the X-ray analysis, the most striking features are structures in the metal distribution. We found two elongated regions of high metallicity in Abell 1758 North with two peaks towards the centre. In contrast, Abell 1758 South shows a deficit of metals in its central regions. Comparing observational results to those derived from numerical simulations, we could mimic the most prominent features present in the metallicity map and propose an explanation for the dynamical history of the cluster. We found in particular that in the metal-rich elongated regions of the North cluster, winds had been more efficient than ram-pressure stripping in transporting metal-enriched gas to the outskirts.
Conclusions. We confirm the merging structure of the North and South clusters, both at optical and X-ray wavelengths.

Key words. X-rays: galaxies: clusters – galaxies: luminosity function, mass function

1. Introduction

Environmental effects are known to have an influence on galaxy evolution, and can therefore modify galaxy luminosity functions (hereafter GLFs). This is particularly obvious in merging clusters, where GLFs may differ from those in non-merging (relaxed) clusters, and where GLFs may also be observed to differ between one photometric band and another (e.g. Boué et al. 2008, and references therein). The GLFs also allow us to trace the cluster-formation history, as shown for example for Coma (Adami et al. 2007).

This dynamical history can also be derived by analysing the temperature and metallicity distributions of the X-ray gas in clusters. These maps have revealed that in many cases clusters with emissivity maps that show a fairly relaxed appearance could have very disturbed temperature and metallicity distributions (see e.g. Boué et al. 2008, and references therein), meaning that they have undergone one or several mergers in the last few Gyr. The study of the thermal structure of the intra-cluster medium (ICM) indeed provides a very interesting record of the dynamical processes that clusters of galaxies have experienced during their formation and evolution. The temperature distribution of the ICM provides insight into the process of galaxy cluster merging and on the dissipation of the merger energy in form of turbulent motion. Metallicity maps can indeed be regarded as a record of the integral yield of all the different stars that have released their metals through supernova explosions or winds during the cluster evolution.

The comparison of temperature and metallicity maps with the results of hydrodynamical numerical simulations allows us to

⋆ Based on archive data retrieved from the Canadian Astronomy Data Centre Megapipe archive and obtained with MegaPrime/MegaCam, a joint project of CFHT and CEA/DAPNIA, at the Canada-France-Hawaii Telescope (CFHT) which is operated by the National Research Council (NRC) of Canada, the Institut National des Sciences de l'Univers of the Centre National de la Recherche Scientifique (CNRS) of France, and the University of Hawaii. The X-ray analysis is based on *XMM-Newton* archive data. This research has made use of the NASA/IPAC Extragalactic Database (NED) which is operated by the Jet Propulsion Laboratory, California Institute of Technology, under contract with the National Aeronautics and Space Administration, and of the SIMBAD database, operated at CDS, Strasbourg, France.

characterize the last merging events that have taken or are taking place. For example, the comparison of the complex temperature and metallicity maps of Abell 85 by Durret et al. (2005) with the numerical simulations by Bourdin et al. (2004) show that two or three mergers have taken place at various epochs in this cluster in the last few Gyr, apart from the ongoing merger seen as a filament made of groups falling onto the cluster (Durret et al. 2003).

We have become interested in pairs of clusters, where the effects of merging are expected to be even stronger. In some cases, one of the clusters itself shows a double structure (Abell 223, Abell 1758 North). By coupling deep optical multiband imaging with X-ray maps, we have recently analysed the Abell 222/223 cluster pair (Durret et al. 2010). We found that Abell 222 (the less perturbed and less massive cluster) had GLFs that were well fit by a Schechter function, with a steeper faint-end in the r' band than in the g' band, which implies little star formation; its X-ray gas showed quite homogeneous temperature and metallicity maps, but with no cool core, which suggests that some kind of merger must have taken place to suppress the cool core. This was confirmed by the distribution of bright galaxies in this cluster, which also suggests that this cluster is not fully relaxed. Abell 223 (the most perturbed and massive cluster) was found to have comparable GLFs in both bands, with an excess of galaxies over a Schechter function at bright magnitudes. Its temperature and metallicity distributions were found to be very inhomogeneous, implying that it has most probably just been crossed by a smaller cluster, which now appears at the north-east tip of the maps. A bridge of galaxies seems to exist between the two clusters (Dietrich et al. 2002) as well as a possible dark-matter filament that joins the two clusters (Dietrich et al. 2005).

The Abell 1758 cluster, at a redshift of 0.279, was analysed in X-rays by David & Kempner (2004) based on Chandra and *XMM-Newton* data. The authors showed that this cluster is indeed a double cluster, with a north and a south component separated by approximately 8 arcmin (2 Mpc in projection), which are both undergoing major mergers with evidence for X-ray emission between the two clusters. However, very little has been published on this system at optical wavelengths, and few galaxy redshifts are available. As a second study of cluster pairs, we chose to analyse this system by coupling archive optical Canada-France-Hawaii Telescope (CFHT) Megacam data with archive *XMM-Newton* data. This allowed us to compute GLFs in two bands as well as temperature and metallicity maps for the ICM, which were compared with the results of numerical simulations.

For a redshift of 0.279, Ned Wright's cosmology calculator[1] (Wright 2006) gives a luminosity distance of 1428 Mpc and a spatial scale of 4.233 kpc/arcsec, giving a distance modulus of 40.77 (assuming a flat ΛCDM cosmology with H_0 = 70 km s^{-1} Mpc^{-1}, $\Omega_M = 0.3$ and $\Omega_\Lambda = 0.7$).

The paper is organised as follows. We describe our optical analysis in Sect. 2 and results for the observed and simulated galaxy luminosity functions in Sect. 3. The X-ray data analysis and results, including temperature and metallicity maps, are presented in Sect. 4. The results of numerical simulations that were run to help us to account for the X-ray temperature and metallicity maps are described in Sect. 5. An overall picture of this cluster pair is drawn in Sect. 6.

[1] http://nedwww.ipac.caltech.edu/

Table 1. Summary of the observations.

Filter	g'	r'
Number of coadded images	4	9
Total exposure time (s)	1800	4860
Seeing (arcsec)	0.75	0.65
Limiting magnitude (5σ)	27.1	26.8

2. Optical data and analysis

2.1. The optical data

We retrieved from the CADC Megapipe archive (Gwyn 2009) the reduced and stacked images in the g' and r' bands (namely G008.203.140+50.518.G.fits and G008.203.140+50.518.R.fits) and give a few details on the observations in Table 1. Observations were made at the CFHT with the Megaprime/Megacam camera, which has a pixel size of 0.186×0.186 arcsec^2.

We did not use the catalogues available for these images, because they were made without masking the surroundings of bright stars, so we preferred to build masks first and then extract sources with SExtractor (Bertin & Arnouts 1996). The total area covered by the images was $20\,403 \times 22\,406$ pixels^2, or 1.05×1.16 deg^2 (16.1×17.6 Mpc^2 at the cluster redshift).

Objects were detected and measured in the full r' image, then measured in the g' image in double image mode (i.e. the objects detected in r' were then measured in g' exactly in the same way as in r'). Magnitudes are in the AB system. The objects located in the masked regions were then taken out of the catalogue, which led to a final catalogue of 298 170 objects. We created masks around bright stars and image defects in the portion of the image covered by Abell 1758 and by the ring around the cluster that was used to estimate the background galaxy contamination to the GLF (owing to its relatively high redshift the cluster does not cover the entire image). After taking out the masked objects we were left with a catalogue of 286 505 objects with measured r' magnitudes, out of which 277 646 also have measured g' magnitudes.

Because the seeing was better in the r' band (see Table 1), we performed our star-galaxy separation in this band.

2.2. Star-galaxy separation

To separate stars from galaxies, we plotted the maximum surface brightness μ_{max} in the r' band as a function of r'. The result is shown in Fig. 1.

The best fit to the star sequence visible in Fig. 1 calculated for $17.75 < r' < 22$ is $\mu_{max} = 0.996r' - 0.524$, with standard deviations on the slope and constant of 0.002 and 0.035 respectively. The point-source (hereafter called "star") sequence is clearly visible for $r' < 22$, with the star saturation showing well for $r' < 17.75$. We will define galaxies as the objects with $\mu_{max}(r') > 17.4$ for $r' < 17.75$, and as the objects above the line of equation $\mu_{max} = 0.996r' - 0.274$ for $r' \geq 17.75$. Stars will be defined as all other objects (see Fig. 1). The small cloud of points observed in Fig. 1 below the star sequence is in fact defects, but represents less than 2% of the number of stars. We thus obtained a star and a galaxy catalogue.

As a check to see up to which magnitude we could trust our star-galaxy separation, we retrieved the star catalogue from the Besançon model for our Galaxy (Robin et al. 2003) in a 1 deg^2 region centred on the position of the image analysed here. This catalogue is in AB magnitudes (as ours) and is corrected for

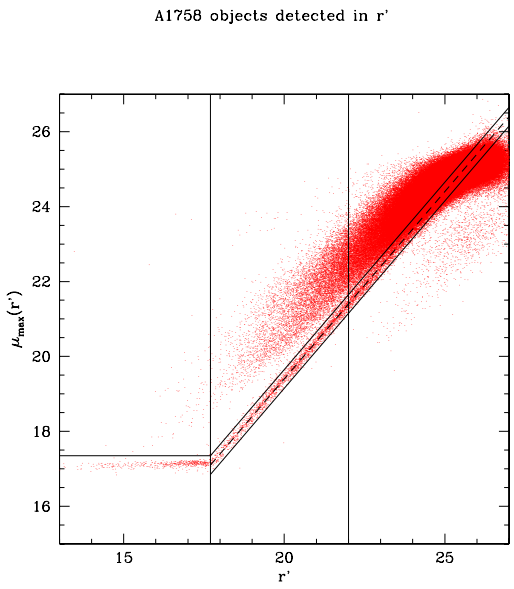

Fig. 1. Central surface brightness in the r' band as a function of r' magnitude. The horizontal and oblique full lines isolate the star sequence (below the horizontal line and between the oblique lines). The two vertical lines correspond to $r' = 17.75$ where the stars stop being saturated, and $r' = 22$, where the fit to calculate the star sequence was limited (see text).

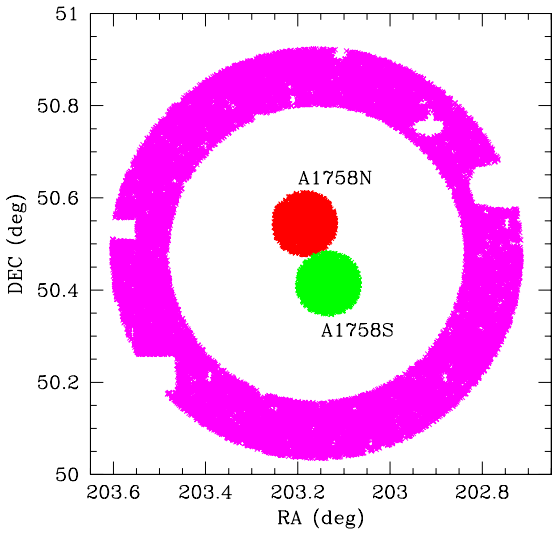

Fig. 2. Positions of the objects (stars and galaxies) in the Abell 1758 North (red) and South (green) catalogues. The objects used to estimate background counts (see text) are shown in magenta. The figure covers 1×1 deg^2 and is slightly smaller than the images.

extinction. To facilitate a comparison with our star catalogue, we corrected our star catalogue (and our galaxy catalogue as well, for later purposes) for extinction: 0.0531 mag in g' and 0.0385 mag in r' (as derived from the Schlegel et al. 1998, maps).

The r' magnitude histogram of the objects classified as stars in our r' image roughly agrees with the Besançon star catalogue for $r' \leq 22$. However, for $r' > 21$, we started to detect more stars than predicted by the Besançon model (the difference is only about 15% at $r' = 21.5$ but becomes 25% in the $r' = 22$ bin, and the difference continues to increase at fainter magnitudes).

We will therefore consider that our star-galaxy separation is correct for $r' \leq 22$. For fainter magnitudes, we computed galaxy counts by counting the total number of objects (galaxies plus stars) per bin of 0.5 mag, and considered the number of galaxies to be equal to the total number of objects minus the number of stars predicted in each bin by the Besançon model.

We extracted from the star and galaxy catalogues two catalogues as large as possible corresponding to the North and South clusters. Their respective positions were taken to be the X-ray centres of the two clusters, as derived from *XMM-Newton* data: 203.1851, +50.5445 (J2000.0, in degrees) for the North cluster, and 203.1335, +50.4138 for the South one. The maximum possible radius to obtain independent catalogues for each of the two clusters was 0.0675 deg, or 1.03 Mpc at a redshift of 0.279.

We obtained three complementary catalogues (with g' and r' magnitudes) for each of the two clusters: objects classified as galaxies (classification valid at least for $r' \leq 22$), objects classified as stars, and a complete catalogue of galaxies+stars, which will be used for $r' > 22$. The positions of the galaxies in the regions of the two clusters are shown in Fig. 2.

2.3. Catalogue completeness

The completeness of the catalogue was estimated by simulations. For this, we added "artificial stars" (i.e. 2D Gaussian profiles with the same full-width-at-half-maximum as the average image point spread function) of different magnitudes to the CCD images and then attempted to recover them by running SExtractor again with the same parameters used for object detection and classification on the original images. In this way, the completeness was measured on the original images.

In practice, we extracted from the full field of view two subimages, each 1300×1300 pixels^2, corresponding to the positions of the two clusters on the image.

In each subfield and for each 0.5 mag bin between $r' = 20$ and 27, we generated and added one star to the image which we then tried to detect with SExtractor, assuming the same parameters as previously. This process was repeated 100 times for each of the two fields and bands.

These simulations give a completeness percentage for stars. This is obviously an upper limit for the completeness level for galaxies, because stars are easier to detect than galaxies. However, we have shown in a previous paper that this method yields a good estimate of the completeness for normal galaxies if we apply a shift of ~0.5 mag (see Adami et al. 2006). Results are shown in Fig. 3.

From these simulations, and taking into account that the results are worse by ~0.5 mag for mean galaxy populations than for stars, we can consider that our galaxy catalogues are complete to better than 80% for $g' \leq 25.8$ and $r' \leq 25.6$ in both clusters.

2.4. Galaxy counts

The surfaces covered by the Abell 1758 North and South catalogues (after excluding masked regions) are 0.01412 deg^2 and 0.01418 deg^2 respectively. Galaxy counts were computed in bins of 0.5 mag normalized to a surface of 1 deg^2.

For $r' \leq 22$, the galaxy counts were derived directly by computing histograms of the numbers of galaxies in the Abell 1758 North and South catalogues. For $r' > 22$, we built for each cluster histograms of the total numbers of objects (galaxies+stars)

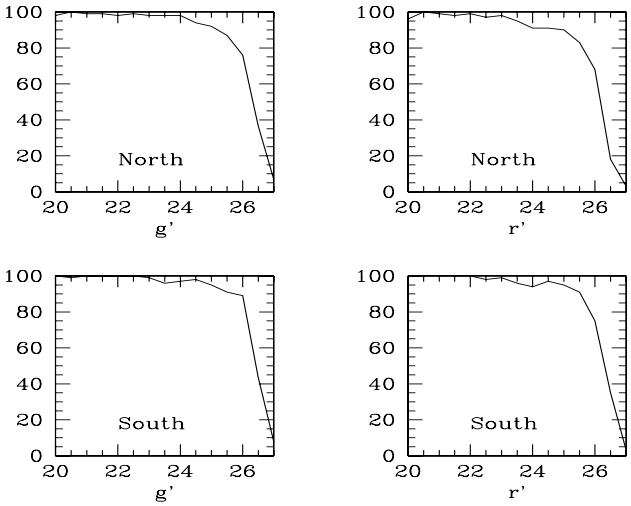

Fig. 3. Point-source completeness as a function of magnitude in percentages for Abell 1758 North (*top*) and South (*bottom*) in g' (*left*) and r' (*right*) for point–like objects (see text).

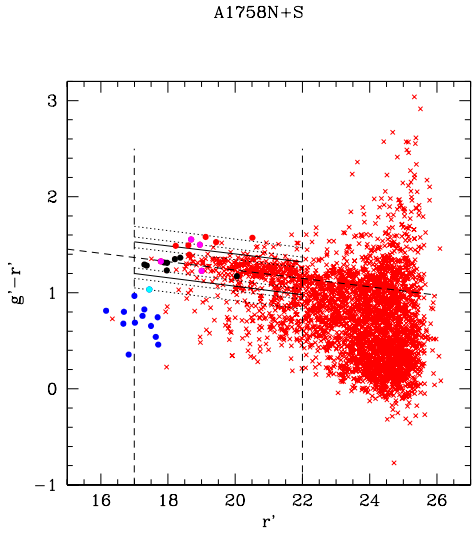

Fig. 4. $(g' - r')$ vs. r' colour–magnitude diagram for Abell 1758 (North and South) for objects classified as galaxies from the $\mu_{\max} - r'$ magnitude relation. The vertical dashed lines indicate the magnitude interval where the colour–magnitude relation was computed. The long oblique dashed line shows the mean colour–magnitude relation; the short oblique dotted lines indicate intervals of $\pm 1\sigma, 2\sigma$ and 3σ around the colour–magnitude relation. The interval finally adopted of 1.5σ is shown with full lines. The filled circles show the galaxies with measured redshifts, colour–coded as follows: black: galaxies belonging to the cluster according to their spectroscopic redshifts, cyan and magenta for galaxies with lower and higher redshifts than the cluster, but inside the two circles where the two clusters were extracted, blue and red: galaxies with lower and higher redshifts than the cluster, but outside these two circles.

and obtained galaxy counts by subtracting the numbers of stars predicted by the Besançon model. The resulting galaxy counts will be used in the next section to derive the GLFs for both clusters in both bands.

As a test, we considered the galaxy counts in the 21.5–22.0 mag bin computed for both clusters with the two methods (i.e. first method: considering that the star-galaxy separation is valid, and second method: considering the total number of objects (galaxies+stars) and subtracting the number of stars predicted by the Besançon model to obtain the number of galaxies). In all cases, the differences are smaller than 4%.

Note that no k-correction was applied to the galaxy magnitudes.

3. Results: colour–magnitude diagrams and galaxy luminosity functions

To compute the galaxy luminosity functions of the two clusters, we need to subtract from the total galaxy counts the number counts corresponding to the contamination by the foreground and background galaxies.

For galaxies brighter than $r' = 22$ we selected galaxies with a high probability to belong to the clusters by drawing colour–magnitude diagrams and selecting galaxies located close to this relation. A few spirals may be missed in this way, but their number is expected to be small in any case, as explained in Sect. 3.1 (also see e.g. Adami et al. 1998). For galaxies fainter than $r' = 22$ we subtracted galaxy counts statistically.

3.1. Colour–magnitude diagram

The $g' - r'$ vs. r' colour–magnitude diagram is shown in Fig. 4 for the two clusters together (the diagrams are the same for both clusters). A sequence is well defined for galaxies in the magnitude range $17 < r' < 22$ in both clusters. We computed the best fit to the $g' - r'$ vs. r' relations in this magnitude range by applying a linear regression. We then eliminated the galaxies located more than 3σ away from this relation and computed the $g' - r'$ vs. r' relation again.

The equation of the colour–magnitude relation is found to be: $g' - r' = -0.0436r' + 2.108$ with an rms on the constant $\sigma = 0.11$.

We also plot in Fig. 4 galaxies with measured spectroscopic redshifts. We can see that the positions of the galaxies belonging to the cluster according to their spectroscopic redshifts, i.e. with redshifts in the [0.264, 0.294] interval, fall very close to the best fit to the colour–magnitude relation.

In view of this, for $r' \leq 22$, we will consider hereafter that all the galaxies located within $\pm 1.5\sigma$ of the colour–magnitude relation (i.e. between the two black lines of Fig. 4) belong to the cluster.

The scatter $\sigma = 0.11$ is somewhat larger than found in the Abell 222/223 clusters at $z = 0.21$ (Durret et al. 2010), but the interval chosen for cluster membership ($\pm 1.5\sigma$) remains smaller than that used, for example, by Laganá et al. (2010) in the redshift interval [0.11, 0.23].

The initial sample of galaxies comprises 1599 and 1438 galaxies in the North and South clusters respectively (with no magnitude limit). Within the $\pm 1.5\sigma$ interval along the red sequence, we are left with respective numbers of galaxies of 477 and 340. These numbers become 192 and 116 galaxies for $r' \leq 22$. The North cluster is obviously richer than the South one.

With this rather strict criterium, we obviously select galaxies with a high probability to belong to the cluster, but we may lose some galaxies, in particular blue cluster galaxies that fall under the sequence.

We therefore estimated the number of blue cluster galaxies lost by selecting galaxies within $\pm 1.5\sigma$ of the red sequence in the following way. First, we computed histograms of numbers of galaxies within $\pm 1.5\sigma$ of the red sequence and below

this sequence in bins of 1 absolute magnitude in the r' band. These counts were made in absolute magnitude bins to be comparable with the counts estimated from luminosity functions of field galaxies. The bins of interest here are between $M_{r'} = -22$ and -19, roughly corresponding to $r' = 18.5$ and 21.5. We then computed the number of foreground galaxies expected. Because the comoving volume at $z = 0.279$ is 5.834 Gpc^3 (Wright 2006) and each of our clusters covers an area of 0.01431 deg^2 on the sky, the volume in the direction of each cluster is 2024 Mpc^3. By using the R-band luminosity function by Ilbert et al. (2005) in the 0.05–0.20 redshift bin (see their Fig. 6 and Table 1), we find that the percentages of "lost" galaxies are of the order of 30% for $M_{r'} = -19$, of 10%–15% for $M_{r'} = -20$ and -21, and less than 10% for brighter galaxies.

3.2. Comparison field

To perform a statistical subtraction of the background contribution for $r' > 22$, and because the cluster is quite distant and does not cover the whole field, we extracted background counts in an annulus surrounding the clusters (see Fig. 2). The annulus was centred on the middle position between the two clusters (203.1593, +50.4792 J2000.0 in degrees), with an inner radius of 0.3232 deg (4.9 Mpc), and an outer radius of 0.4444 deg (6.8 Mpc). The unmasked surface of the annulus is 0.278 deg^2.

We checked if there could be any contamination of background counts in this annulus by a group or cluster, and found a structure west-southwest of Abell 1758. This appears as a cluster in Simbad[2] with the coordinates 13h34mn45.41s, +50°26′01.4″ (J2000.0) and redshift 0.085. The mean redshift for the 20 galaxies extracted from NED (http://nedwww.ipac.caltech.edu/) in this region is 0.0869, with a dispersion in redshift $\sigma_z = 0.0015$. This cluster falls just outside the annulus that was used to estimate the background counts subtracted from the galaxy counts to compute the GLF, so its presence should not modify the galaxy counts inside the annulus.

We can note from Fig. 5 that galaxy counts are comparable in Abell 1758 North and South in the g' band, but differ in the r' band, where Abell 1758 North has more galaxies in the $22 \leq r' \leq 24$ magnitude range.

3.3. Galaxy luminosity functions

The galaxy luminosity functions (GLFs) of Abell 1758 North and South were calculated in bins of 0.5 mag and normalized to 1 deg^2. We subtracted the background contribution using as background galaxy counts the "local" counts in the annulus shown in magenta in Fig. 2.

The GLFs are displayed for Abell 1758 North and South in Figs. 6 and 7 respectively (red points). The error bars drawn in these figures were taken to be 4 times the Poissonian errors on galaxy counts, as derived from detailed simulations previously performed by our team for similar data (see Boué et al. 2008, Fig. 5).

The GLFs (as a function of absolute magnitude) were fit by a Schechter function:

$$S(M) = 0.4 \ln 10 \, \phi^* \, y^{\alpha+1} \, \mathrm{e}^{-y}$$

with $y = 10^{0.4(M^*-M)}$.

The parameters of the Schechter function fits of the GLFs are given in Table 2. The absolute magnitude ranges considered

[2] http://simbad.u-strasbg.fr/simbad/

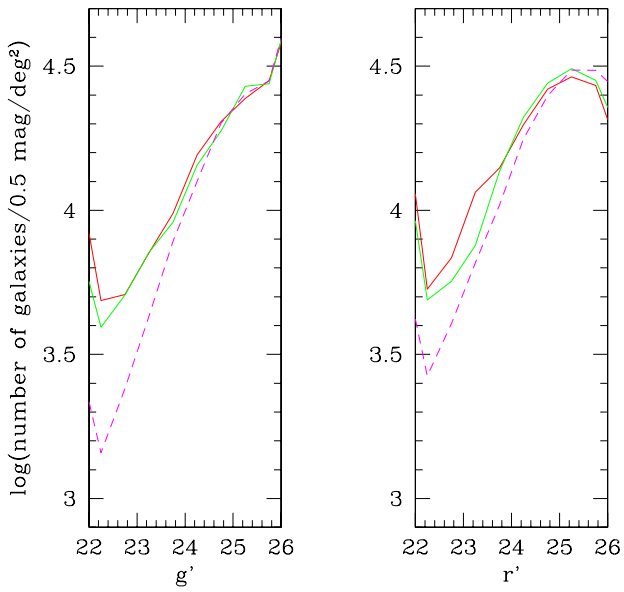

Fig. 5. Galaxy counts in the g' (*left*) and r' (*right*) bands for magnitudes $r' > 22$ where the background must be subtracted statistically, in logarithmic scale. The counts in Abell 1758 North and South are drawn in red and green respectively. The magenta dashed lines show the galaxy counts from the "local" background extracted in the annulus shown in Fig. 2. Error bars are Poissonian and are not plotted for clarity.

are indicated for each fit, and GLFs and their fits are drawn in Figs. 6 and 7.

If we look at Abell 1758 North (Fig. 6), we see that a Schechter function fits most of the GLF points for both bands fairly well. However, there is an excess of galaxies over a Schechter function in the very brightest magnitude bins, specially in the r' band. There is also a "bump" around r' absolute magnitudes -17 and -17.5, which has no obvious explanation. Except for this feature, the GLFs are quite similar in both bands, and the faint-end slopes are quite flat: $\alpha = -0.85$.

In contrast, the GLFs for Abell 1758 South (Fig. 7) are not well fit by Schechter functions. There is a strong excess of galaxies at bright magnitudes in the g' band, and the faint-end slope is quite flat ($\alpha = -0.59$), implying that star formation is weak in faint galaxies of the South cluster. In the r' band, the GLF also shows an excess at very bright magnitudes and a strong dip for $M_{r'} \sim -17.5$. This dip is also visible in the g' band around -17, though it is not as pronounced as in the r' band. In the South cluster the GLFs in the g' and r' bands have quite different faint-end slopes: $\alpha = -0.59$ in g' and $\alpha = -1.11$ in r'. This lack of blue faint galaxies could suggest that star formation has been quenched by a process linked to the merger, but could also be an artefact caused by the method used here to derive the GLF (see end of Sect. 3.4).

The fact that both clusters have GLFs differing from simple Schechter functions is most probably because both are undergoing merging processes, as already pointed out by David & Kempner (2004) from their X-ray study. We will discuss these results in the next section when considering the temperature and metallicity distributions of the X-ray gas. These maps confirm that both clusters are indeed structures that are strongly perturbed by several mergers, so it is not surprising to see effects on the GLFs.

Altogether, the GLFs in Abell 1758 do not strongly differ from those derived in other clusters. The bright parts of the GLF Schechter fits ($M_{r'} < -19$) for both clusters are quite similar in

Table 2. Schechter parameters for galaxy luminosity functions.

Cluster	Filter	Range	Φ^*	M^*	α
North	g'	$[-22.0, -16.5]$	4384 ± 462	-20.06 ± 0.12	-0.86 ± 0.05
	r'	$[-23.5, -16.0]$	4650 ± 286	-21.18 ± 0.08	-0.85 ± 0.02
South	g'	$[-22.0, -15.5]$	5319 ± 574	-18.90 ± 0.14	-0.59 ± 0.08
	r'	$[-23.5, -16.0]$	1582 ± 229	-21.34 ± 0.16	-1.11 ± 0.04
North	g'	$[-22.0, -16.5]$	3244 ± 236	-20.33 ± 0.09	-1.00 ± 0.02
	r'	$[-23.5, -16.0]$	3451 ± 229	-21.44 ± 0.08	-0.96 ± 0.02
South	g'	$[-22.0, -15.5]$	1652 ± 205	-20.09 ± 0.16	-1.12 ± 0.03
	r'	$[-23.5, -16.0]$	1849 ± 195	-21.18 ± 0.14	-1.06 ± 0.03
Simulated		$[-25.0, -15.0]$	755 ± 21	-22.09 ± 0.04	-1.01 ± 0.01

Notes. The first set of fits corresponds to galaxies selected from the colour–magnitude relation for $r' < 22$ and to a statistical background subtraction with galaxy counts taken from the CFHTLS Deep field counts for $r' > 22$. The second set of fits corresponds to galaxies selected from the colour–magnitude relation at all magnitudes. The last line corresponds to the fit to the simulated GLF (see text).

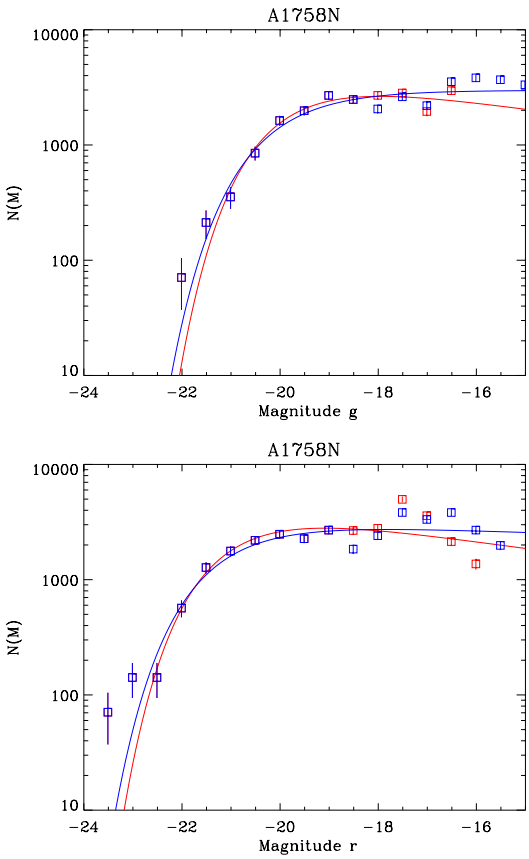

Fig. 6. Galaxy luminosity functions for Abell 1758 North in the g' (*top*) and r' (*bottom*) bands, in logarithmic scale. The blue and red points correspond to the two galaxy selections (see text), and the best Schechter function fits are drawn with the same colours as the corresponding points. At bright magnitudes the points exactly coincide, and because the blue points were plotted after the red ones, they appear blue. Error bars are 4 times the Poissonian errors on galaxy counts (see text).

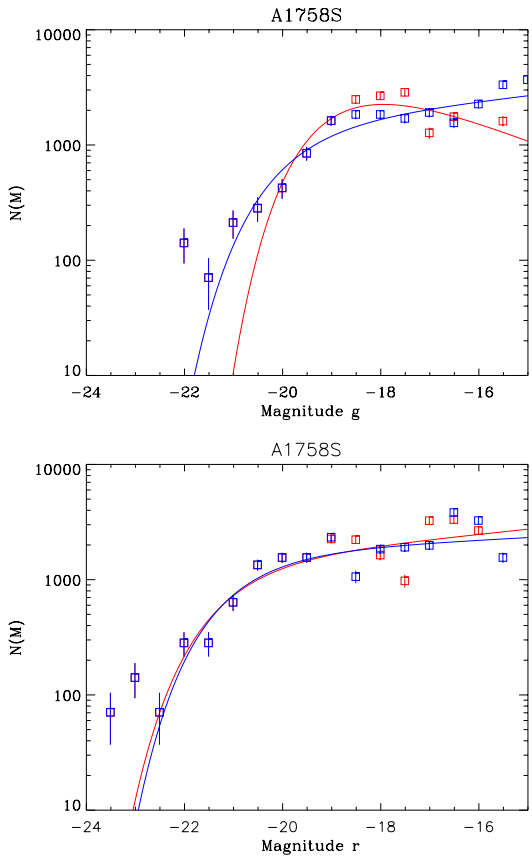

Fig. 7. Same as Fig. 6 for the South cluster.

shape to the GLFs recently obtained by other authors (see for example Andreon et al. 2008). And the faint-end slopes are within the broad range of values estimated by previous authors for different clusters, cluster regions, and photometric bands (see e.g. the compilation in Table A1 of Boué et al. 2008), except for the South cluster in the g' band, where the GLF seems unusually flat.

Abell 1758 is at redshift 0.279, and few GLFs are available for clusters at these redshifts. Andreon et al. (2005) found more or less comparable faint-end slopes of -1.03 and -1.30 for two clusters at redshifts ∼0.3, but in the K band, which makes the comparison with our results not straightforward.

3.4. Galaxy luminosity functions only based on a colour–magnitude selection

As a test to our method, we also derived the GLFs by considering that all galaxies located within $\pm 1.5\sigma$ of the colour–magnitude relation shown in Fig. 4 were cluster members, for all magnitudes.

The corresponding points and GLF Schechter fits are shown in blue in Figs. 6 and 7 and the corresponding Schechter parameters are given in the second half of Table 2. Obviously the data

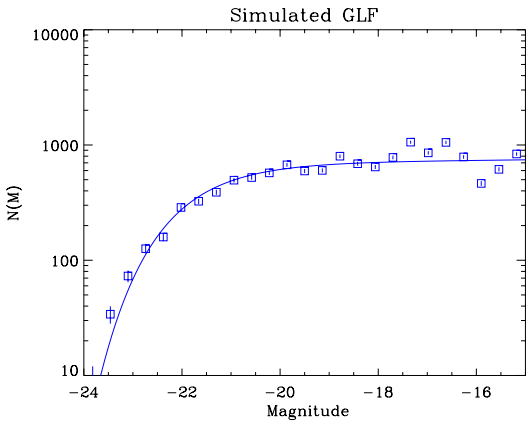

Fig. 8. Simulated luminosity function with best Schechter fit superimposed.

points of the GLFs start to differ for absolute magnitudes fainter than about −19 to −18. The agreement between the Schechter fits based on the two methods is fair for the North cluster in both bands and for the South cluster in the r' band, though the Schechter parameters found in corresponding cases are not always within error bars. This strongly suggests that the errors on these parameters are underestimated, and this is probably also the case for the errors on the GLF points themselves. But the agreement is poor for the South cluster in the g' band. Therefore we cannot consider that the g' band GLF is well constrained in the South cluster.

These results clearly illustrate the difficulty to estimate GLFs, particularly at faint magnitudes, as already mentioned by a number of authors (see discussion in Durret et al. 2010). They also justify our choice not to attempt GLF fits with a higher number of free parameters, as would be obtained by fitting a Gaussian at bright magnitudes plus a Schechter function at faint magnitudes, or two Schechter functions.

3.5. Simulated galaxy luminosity function

In connection with the numerical simulations presented in Sect. 5, we simulated a galaxy luminosity function using the halo mass–luminosity relation from Vale & Ostriker (2006). The halo mass for the simulated galaxies is taken from the galaxy formation model, which calculates the halo mass from the N-body simulation. All the simulated galaxies were put into 25 mag bins between absolute magnitudes −25 and −15.

The resulting GLF is shown in Fig. 8. We can see that it appears quite similar in shape to those shown in Figs. 6 and 7. A Schechter fit to this function is superimposed in Fig. 8 and its parameters are given in Table 2. We can see that although the value of M^* is between half a magnitude and a magnitude brighter, the faint-end slope agrees well with the values derived from the observations.

3.6. Do the North and South clusters have a cD galaxy?

The images of the three brightest galaxies of each cluster are shown in Fig. 9. We can see that in the North cluster none of these galaxies is at the cluster centre, and there are obviously two subclusters. In the South cluster, none of the three brightest galaxies is perfectly in the centre either (the galaxy that is not circled is a foreground object).

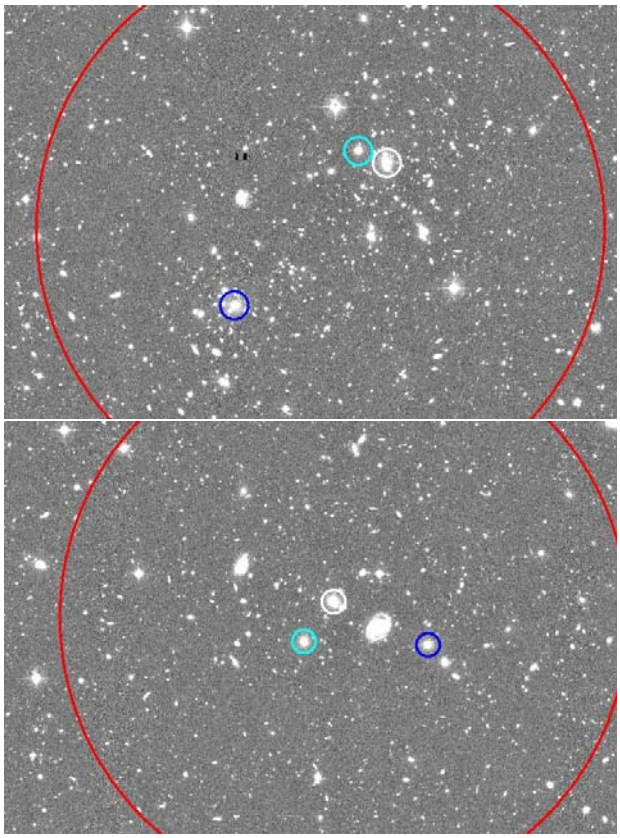

Fig. 9. Optical images of Abell 1758 North (*top*) and South (*bottom*). For each cluster, the brightest galaxy is circled in white, the second brightest in blue and the third brightest in cyan. The red circles show the cluster limits. The uncircled galaxy near the centre of the South cluster is a foreground object.

The similarity with the Abell 222/223 cluster pair (see Durret et al. 2010, Fig. 20) has led us to analyse the brightness profiles of the brightest galaxies in the Abell 1758 North and South clusters. We had found that Abell 223 (which resembles Abell 1758 North) had two brightest cluster galaxies (BCGs), one of them showing a brightness profile decreasing slower than the other, and therefore resembling that of a cD, while the other one could be the central galaxy of an accreted group.

The surface brightness profiles of the three brightest galaxies in the two Abell 1758 clusters are displayed in Fig. 10. Evidently the profiles of the two brightest galaxies of the North cluster decrease notably slower with radius that those of the other bright galaxies, and surprisingly, the profile of the second brightest galaxy is much flatter than that of the brightest one. This suggests that there are two dominant galaxies in the North cluster, quite similar to what was seen in Abell 223, and this is another indication of a merger. That there are probably two dominant galaxies is another indication of a merger of two smaller systems, which agrees with David & Kempner (2004), who suggested that at least two smaller clusters have crossed this North system. But there is no dominant galaxy in the South cluster, where the profiles of the three brightest galaxies are similar.

4. X-ray analysis

We present in Fig. 11 the X-ray surface brightness isocontours overplotted on the optical r' band image of Abell 1758 and indicate the positions of the three brightest galaxies of each cluster. The three galaxies of each cluster are the remaining central

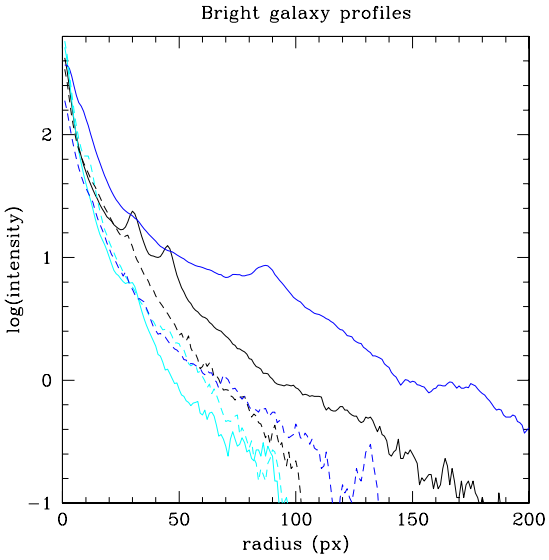

Fig. 10. Surface brightness profiles of the three brightest galaxies in both clusters (intensities are normalized to the central value and in arbitrary units, and radii are in pixels). Full and dashed lines correspond to galaxies in the North and South clusters respectively. For each cluster, the brightest galaxy is in black, the second brightest in blue and the third brightest in cyan.

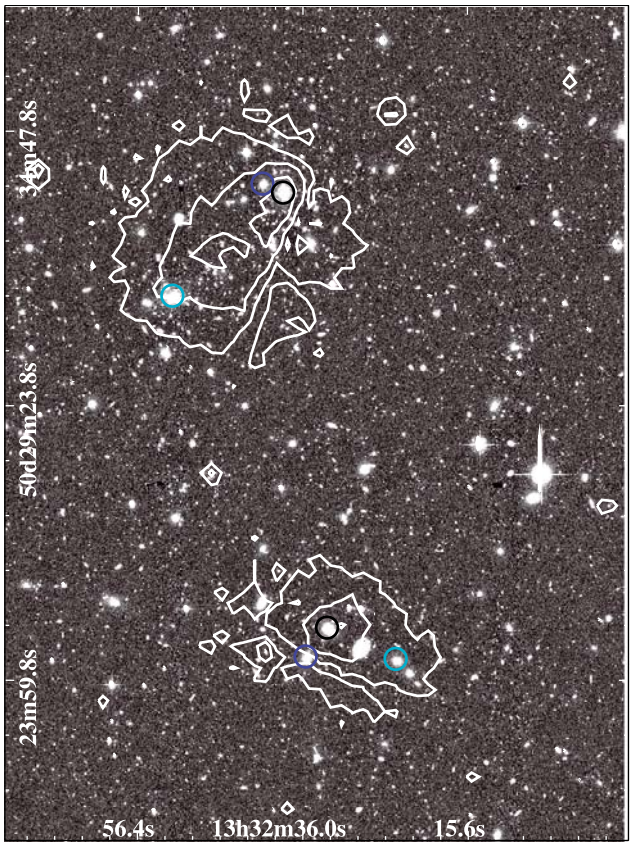

Fig. 11. Optical image with X-ray isocontours superimposed. The circles correspond to the three brightest galaxies in Abell 1758 North. The colours are the same as in Fig. 10: the brightest galaxy is in black, the second brightest in blue and the third brightest in cyan.

galaxies from the ancient sub-clusters. Another important aspect to notice is their position: the two brightest galaxies are one near the other and the third one is radially opposite. This is an indication of a recent merger where we clearly see that while the gas has already settled down, the brightest galaxies are not in the centre of Abell 1758 North and A1758 South. We will revisit this merging scenario in the following sections.

4.1. Data reduction

Abell 1758 was observed for ~57 ks with *XMM-Newton* with the medium filter inserted. The *XMM-Newton* ODF files were processed using SAS version v8.0. The MOS and pn files were filtered excluding all events with FLAG > 0 and PATTERN > 12, and FLAG > 0 and PATTERN > 4, respectively. Light curves were made in the 1–10 keV energy band, and periods where the background value exceeded the mean value by more than 3σ were excluded. We considered events inside the field of view (FOV) and excluded all bad pixels. Flare filtering left life-times of 16928 s, 12734 s, and 16929 s in the MOS1, MOS2, and pn cameras respectively.

The background was taken into account by extracting MOS1, MOS2, and pn spectra from the publicly available EPIC blank sky templates of Andy Read (Read & Ponman 2003). The background was normalized using a spectrum obtained in an annulus (between 12.5–14 arcmin) where the cluster emission is no longer detected.

4.2. Spectrally measured 2D X-ray maps

We performed quantitative studies using X-ray spectrally measured 2D maps to derive global properties of these two clusters. These maps were made in a grid; for each spatial bin we set a minimum count number of 900 (after background subtraction). For the spectral fits, we used XSPEC version 11.0.1 (Arnaud 1996) and modelled the obtained spectra with a MEKAL single temperature plasma emission model (bremsstrahlung + line emission Kaastra & Mewe 1993; Liedahl et al. 1995). The free parameters are the X-ray temperature (kT) and the metal abundance (metallicity). Spectral fits were made in the energy interval of 0.7−8.0 keV with the hydrogen column density fixed at the Galactic value (1.06×10^{20} cm^{-2}), estimated with the nH task of FTOOLS (based on Dickey & Lockman 1990).

We computed the effective area files (ARFs) and the response matrices (RMFs) for each region in the grid. This procedure (already described in Durret et al. 2010) allows us to perform a reliable spectral analysis in each spatial bin to derive high-precision temperature and metallicity maps, because we simultaneously fit all three instruments. The best-fit value is then attributed to the central pixel.

The resulting X-ray temperature and metallicity maps are displayed in Figs. 12 and 13. Maps of the errors on these two maps are given in the appendix (Fig. A.1).

The temperature maps in Fig. 12 show that both clusters appear almost isothermal, the North one being hotter (~6–7 keV) and the South one being cooler (~4–5 keV). The presence of inhomogeneities is not obvious in the temperature maps, except for a hotter blob in the northwest region of Abell 1758 North. Although signs of recent interactions are not clearly present in the temperature map, the positions of the three brightest galaxies argue in favour of a merging scenario where two clusters merged to form Abell 1758 North, as mentioned in Sect. 4.

But two striking aspects draw our attention when considering the metallicity map shown in Fig. 13. First, there are two elongated regions of high metallicity in the North cluster, which suggest that at least two smaller clusters have crossed the North

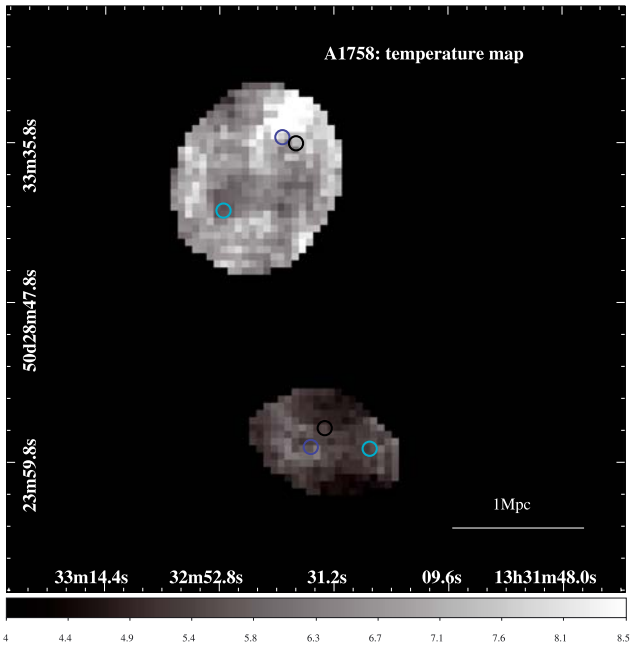

Fig. 12. X-ray temperature map for Abell 1758 North (*top*) and South (*bottom*). The colour–bar indicates the temperature in keV. The circles correspond to the three brightest galaxies in each cluster. The colours are the same as in Fig. 10: the brightest galaxy is in black, the second brightest in blue and the third brightest in cyan. The corresponding error map is shown in Fig. A.1 (*top*).

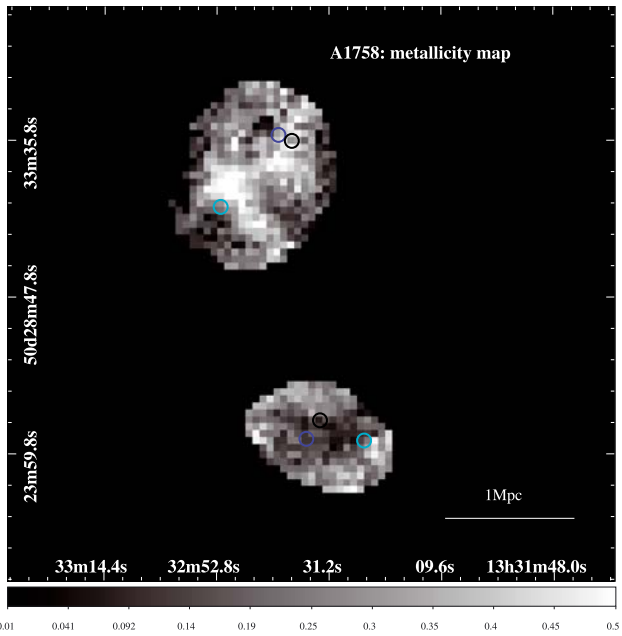

Fig. 13. X-ray metallicity map for Abell 1758 North (*top*) and South (*bottom*). The colour–bar indicates the metallicity in solar units. The circles correspond to the three brightest galaxies in each cluster. The colours are the same as in Fig. 10: the brightest galaxy is in black, the second brightest in blue and the third brightest in cyan. The corresponding error map is shown in Fig. A.1 (*bottom*).

cluster (as pointed out by David & Kempner 2004). Based on the positions of the three brightest galaxies we can assume a scenario in which metals in these elongated regions were left by ram-pressure stripping during the merger.

Second, the metallicity map of the South cluster is even more unusual, because it shows a deficit of metals in the central region. This deficit is probably the signature of an interaction with the central object. Because this cluster is less massive, the effects of galactic winds or supernova explosions will be stronger to expell metals towards the outskirts (Evrard et al. 2008).

However, none of the metal structures identified in the 2D maps correlates with any temperature structure for either cluster. We do not see the high-metallicity regions of the North cluster in the temperature map.

To have an overview of the merging scenario and better understand the dynamical history of these clusters, we considered the results of numerical simulations to give support to our findings, and compared them with our observational results. This will be presented in the next section.

David & Kempner (2004) have already analysed this system using *XMM-Newton* and *Chandra* data. They concluded that these two clusters most likely form a gravitationally bound system, though their imaging and spectroscopic analyses do not reveal any sign of interaction between the North and South clusters and show that A1758N and A1758S are both undergoing major mergers. It is clear from our analysis that Abell 1758 North is still undergoing at least one merger, the bright and hot zone seen in the temperature map probably is the signature of one of the cores. For Abell 1758 South, the merger is not evident in X-rays, though some kind of interaction is suggested by the absence of a cool core and is confirmed by the optical data analysis.

5. Numerical simulation results

As described in detail in Kapferer et al. (2006), Kapferer et al. (2007), or Schindler et al. (2005) we combine several codes to model the metal distribution in a galaxy cluster. To calculate the dark-matter structure of the galaxy cluster, we use the *N*-body code GADGET2 (Springel 2005) with constrained random fields as initial conditions (Hoffman & Ribak 1991). A semi-analytical galaxy-formation model then assigns galaxy properties to the halos found in the dark-matter structure. For this galaxy-formation model we use an improved version of the code described by van Kampen et al. (1999). The chemical evolution of the galaxies is modelled as in Matteucci & François (1989). To study the evolution of the ICM, we use a hydrodynamic grid code with comoving coordinates and a PPM-scheme for a better treatment of shocks (Colella 1984). To optimize the computational time, we use four nested grids (Ruffert 1992), each with $128 \times 128 \times 128$ cells. The total computational hydro-volume has a side length of 20 Mpc. We included special routines to transport enriched material out from the modelled galaxies into the ICM: we model ram-pressure stripping (Gunn & Gott 1972) as well as galactic winds as described in Domainko & Kapferer (2006), and Kapferer et al. (2007). More specifically, the ram-pressure and galactic wind algorithms calculate a mass loss for each model galaxy (depending on its velocity with respect to the ICM and its star-formation rate). Because the galaxy formation model provides us with the metallicity within the ISM, we know the quantity of metals transported from the ISM into the ICM. These metals are then advected with the ICM, and by knowing the ICM density we can then calculate the ICM metallicity. Combining these codes, we can simulate the 3D evolution of the ICM and its metallicity. From these 3D data we extract temperature and metal maps by deriving emission-weighted projections. These maps can be compared directly with the observations.

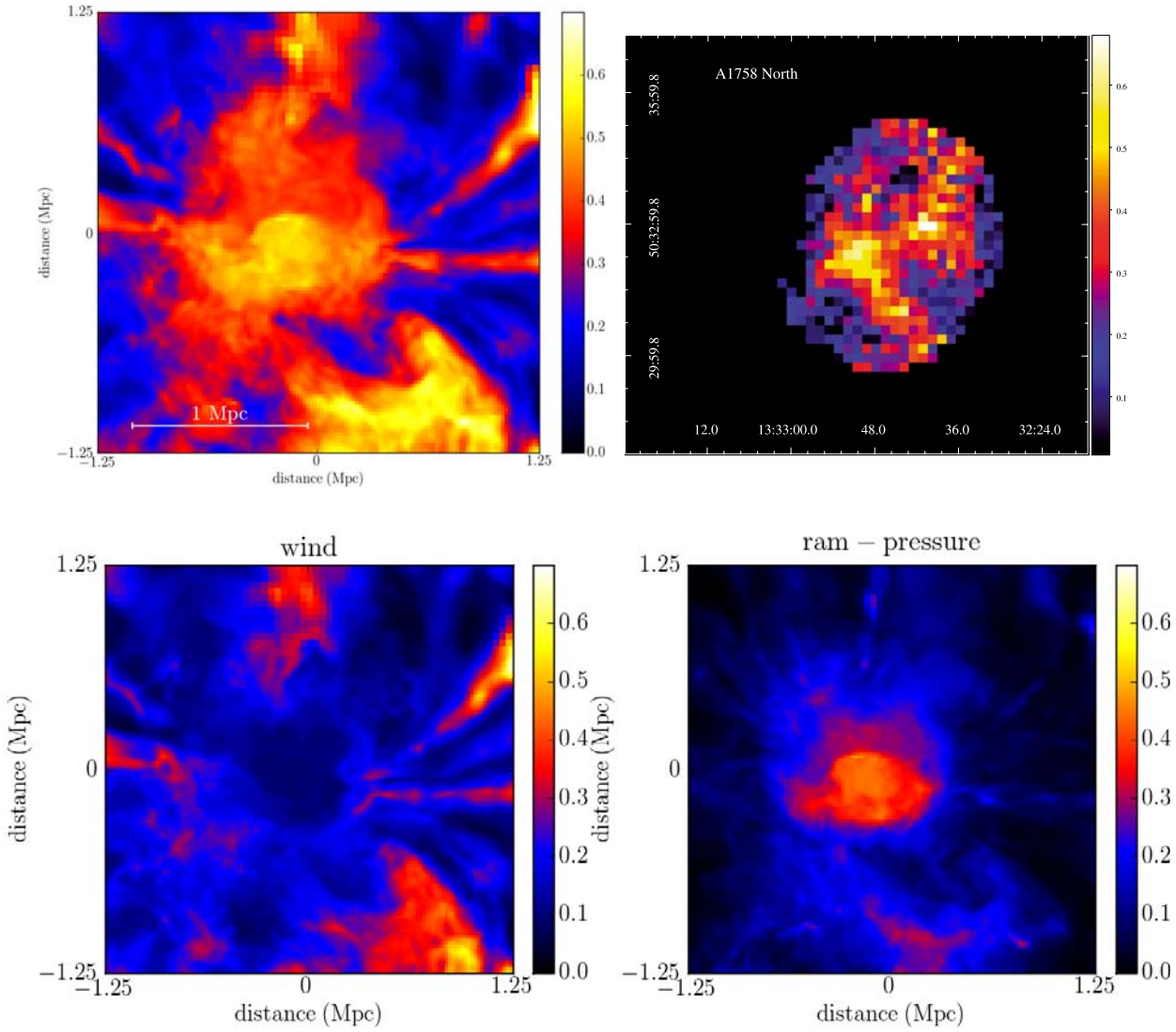

Fig. 14. *Top left panel*: metal distribution predicted by numerical simulations at the cluster redshift (i.e. sum of the two panels below). *Top right panel*: observed metal distribution map in Abell 1758 North. Both panels have a side-length of 2.5 Mpc. *Bottom left panel*: metals that were ejected by galactic winds. *Bottom right panel*: metals that were transported out of the galaxies by ram-pressure stripping.

We performed five simulations with different initial conditions and selected the simulation that best matched our observational results. We did not set up the simulations to specifically reproduce Abell 1758. Among all the tests performed here, we found one metal distribution that quite reasonably reproduces the elongated region of high abundance found observationally for the North cluster. We see that the simulated 2D map in Fig. 14 can also reproduce the exact values for the metallicity of the North cluster. For the bright regions (in yellow colour) we derived metallicity values of about 0.5–0.6 solar units. The metallicity decreases towards the outskirts, where it reaches values around 0.2 solar units.

It is very important to mention the spatial scales of the features presented in the 2D metal distribution maps predicted by numerical simulations and derived from observations. The physical sizes of the two top panels in Fig. 14 are exactly the same (a side-length of 2.5 Mpc), but the features, although similar in shape, do not have the same physical sizes. In the observational metal distribution (top right panel in Fig. 14) we see that Abell 1758 North is completely comprised within 2.5 Mpc, while in the metal distribution computed from numerical simulations (top left panel in Fig. 14) the cluster extends over a larger region. The point here is that we did not make the simulations to exactly match this cluster.

To analyse the importance of galactic winds and ram-pressure stripping in transporting metals, we display in Fig. 14 the results of numerical simulations, which separately show the metals that are ejected by galactic winds (bottom left), those transported out of the galaxies by ram-pressure stripping (bottom right), and the sum of the metals accounted for by these two processes (top left). These maps can be compared with the metallicity map derived from observations for the North cluster (top right). From these figures, we can say that both processes are important for metal enrichment and play different roles in the cluster, with winds definitely playing a higher part in the south-west corner. Galactic winds are more important in the outskirts of the cluster, while ram-pressure stripping seems to be dominant in the inner parts.

The time scales of these different enrichment processes are also remarkable. By analysing the results of our numerical simulation, we can say that a large part of the metals for the high-metallicity region in the south of Abell 1758 North and the thin elongated stripe from the centre to the north-west have been transported into the ICM at redshifts $z > 3$. Then, there was a substantial contribution to the metallicity in the elongated structure between redshifts 3 and 2 but no contribution to the centre of the cluster. Between redshifts 2 and 1, there was a substantial contribution to the central region (around 1/3 of the final metallicity), mainly from ram-pressure. Then, there was hardly any contribution to the metallicity at all between redshifts 1 and 0.8. From $z = 0.8$ to $z = 0.5$ there was a contribution (around 0.2 solar metallicities) to the metals in the central region, only from ram-pressure stripping. And finally, from $z = 0.5$ to $z = 0.279$ (the cluster redshift) there was hardly any significant contribution to the metallicity. In summary, many of the metals that are responsible for the features in the outskirts have been transported into the ICM at very early times, even before $z = 3$. If we look at the metals that have been transported into the ICM before $z = 2$, we see that they explain the main morphological features in the outskirts (such as the elongated structure). Yet the enrichment of the central region takes place mainly between $z = 2$ and $z = 0.5$, predominantly via ram-pressure stripping.

The results presented above show that the comparison of observations with the results of numerical simulations is a powerful tool to better understand the physical processes involved in the transport of metals. However, there is still work to be done on this topic, based on a larger sample of clusters in different dynamical states.

6. Discussion and conclusions

Clearly, clusters are in a continual state of evolution, and with high-precision telescopes such as *XMM-Newton* and *Chandra*, we see that they are hardly ever relaxed and virialized as was previously assumed. We have thus become interested in multiple mergers, where merging effects are expected to be even stronger.

As a second study of cluster pairs, we chose to analyse Abell 1758 (at a redshift of 0.279) by coupling archive optical CFHT Megacam and *XMM-Newton* data, and by comparing the temperature and metallicy maps obtained for the ICM with the results of numerical simulations. We added to this by also considering the results of numerical simulations to try to better understand the dynamics and evolutionary history of this system.

From our results, signs of merger(s) are detected in the optical and the X-ray wavelength ranges, meaning that both galaxies and gas are still out of equilibrium. From the optical results we see that for Abell 1758 North, a Schechter function fits most of the points of the GLFs in the g' band fairly well, but there is an excess of galaxies over a Schechter function in the brightest magnitude bins, specially in the r' band, as well as a possible and unexplained excess of galaxies around $M_{r'} \sim -17.5$. In contrast, for Abell 1758 South, which is metal-poorer than the North cluster, the GLF is not as well defined and fit by a Schechter function. Especially the GLFs derived by the two methods (statistical background subtraction for $r' > 22$ or colour–magnitude selection at all magnitudes) look quite different, particularly in the g' band. If the dip detected in the r' band GLF for $M_{r'} \sim -18$ is real, as already found in other clusters but at somewhat brighter absolute magnitudes, it could be interpreted as showing the transition zone between (brighter) ellipticals and (fainter) dwarfs (Durret et al. 1999). An excess of galaxies over a Schechter function in the brightest magnitude bins is observed in both bands. Furthermore the GLFs in the g' and r' bands look quite different in the South cluster, with a faint-end slope somewhat steeper in r' than in g'. The shallower faint-end slope in g', if real, could be explained either by quenching of star formation by the merger (which strips galaxies from their gas and reduces star formation), or because star formation has not yet had time to be triggered by the merger (see e.g. Bekki 1999). The somewhat perturbed shapes of the GLFs of both clusters therefore agree with the assumption that they are both undergoing merging processes.

From the X-ray analysis we noticed that the gas temperature maps do not present prominent inhomogeneities, except for a hotter blob in the northwest of Abell 1758 North. The North cluster is hotter (with temperatures in the range of ∼6−7 keV) and the South one cooler (with $kT \sim 4$−5 keV). The hotter blob in the northwest of Abell 1758 North could be explained by heating of the gas in that region by the movement of the northwest system towards the north proposed by David & Kempner (2004). The most striking features are seen in the metallicity maps. The metallicity map of the South cluster is even more unusual, because it shows a deficit of metals in the central region. This deficit is probably the signature of an interaction with the central object that could have expelled metals towards the outskirts (see Evrard et al. 2008, and top left panel of Fig. 14). We also detect two elongated regions of high metallicity in the North cluster, suggesting that at least two smaller clusters have crossed the North cluster. Our temperature and metallicity maps agree with the scenarios proposed by David & Kempner (2004), who derived that the North cluster is in the later stages of a large impact parameter merger between two 7 keV clusters, while the south cluster is in the earlier stages of a nearly head-on merger between two 5 keV clusters.

To better understand the nature of the most prominent features exhibited in the metallicity map of the North cluster, we performed five simulations with different initial conditions. It should be stressed that we did not set up the simulations to specifically reproduce Abell 1758. Among these five simulations, we found one metal distribution that quite reasonably reproduces the elongated region of high abundance found observationally for the North cluster, although without a perfect spatial correlation. The results of our numerical simulations allowed us to distinguish the role of metal transportation processes such as galactic winds and ram-pressure stripping. We showed that these phenomena act in different regions of the cluster, and that in the metal-rich elongated regions of the North cluster winds were more efficient in transporting enhanced gas to the outskirts than ram-pressure stripping. These simulations also allowed us to compute the GLF, and the result is consistent with the observed GLFs.

In the hope of finding some kind of large-scale structure and/or filaments linking Abell 1758 with its surroundings, we searched the NED database for galaxies with redshifts available in a region of 36 arcmin around Abell 1758 (corresponding to 9.1 Mpc at the cluster distance). We found 137 galaxies, out of which only 15 have redshifts in the approximate cluster redshift range: [0.264, 0.294]. No structure was found in the blueshifted and redshifted galaxies, except for what appears to be a cluster west of Abell 1758 (see Sect. 3.2). Therefore we cannot derive any argument from the large-scale distribution of galaxies around Abell 1758.

To conclude, the Abell 1758 North and South clusters most likely form a gravitationally bound system, but our imaging analyses of the X-ray and optical data do not reveal any sign of interaction between the two clusters. All signs of dynamical

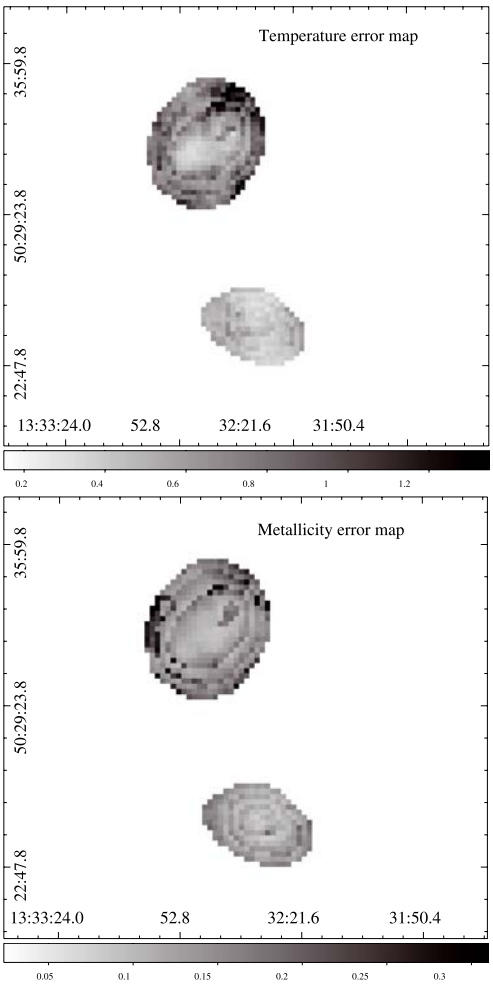

Fig. A.1. *Upper panel*: error map on the X-ray temperature. *Lower panel*: error map on the X-ray metallicity.

disturbance are associated with recent merger(s) that each of the two clusters is still undergoing.

Acknowledgements. We are grateful to Christophe Adami, Gastão B. Lima Neto and Sabine Schindler for discussions. We warmly thank Andrea Biviano for giving us his Schechter function fitting programme and helping us with the corresponding plots. Thanks also to Thad Szabo for sending us information before publication. F.D. acknowledges long-term support from CNES. T.F.L. acknowledges financial support from FAPESP (grants: 2006/56213-9, 2008/04318-7). M.H. is grateful to the Austrian Science Foundation (FWF) through grant number P19300 and for support by the Austrian Ministry of Science BMWF as part of the UniInfrastrukturprogramm of the Forschungsplattform Scientific Computing at the LFU Innsbruck. Finally, we acknowledge the referee's interesting and constructive comments.

Appendix A: Error maps

In Fig. A.1 we present the errors associated to each bin in the temperature and metallicity maps displayed in Figs. 12 and 13. The errors on these parameters were directly obtained from the spectral fits.

Looking at Figs. 12, 13 and A.1 (error maps) we see that, for the temperature estimates, we have errors around 5% for A1758 South, while for A1758 North they vary from 5% (in the inner parts) up to 12% (at the outskirts). The errors on the temperature maps are therefore very reasonable. For the metallicity maps we do not have the same accuracy. Looking at the same figures, we see that for A1758 South, the metallicity errors can reach 25% and for A1758 North they vary from 30% (in the inner region) up to 46% (at the outskirts). It is important to notice that although the *XMM-Newton* exposure time on Abell 1758 was about 57 ks, due to flare filtering only ≈17 ks of good data were useable to construct the 2D spectral maps.

References

Abazajian, K. N., Adelman-McCarthy, J. K., Agüeros, M. A., et al. 2009, ApJS, 182, 543.
Adami, C., Biviano, A., & Mazure, A. 1998, A&A, 331, 439
Adami, C., Picat, J.-P., Savine, C., et al. 2006, A&A, 451, 1159
Adami, C., Durret, F., Mazure, A., et al. 2007, A&A, 462, 411
Andreon, S., Punzi, G., & Grado, A. 2005, MNRAS, 360, 727
Andreon, S., Puddu, E., de Propris, R., & Cuillandre, J.-C. 2008, MNRAS, 385, 979
Arnaud, K. A. 1996, ASPC, 101, 17
Bekki, K. 1999, ApJ, 510, L15
Bertin, E., & Arnouts, S. 1996, A&AS, 117, 393
Boué, G., Adami, C., Durret, F., Mamon, G., & Cayatte, V. 2008, A&A, 479, 335
Bourdin, H., Sauvageot, J.-L., Slezak, E., Bijaoui, A., & Teyssier, R. 2004, A&A, 414, 429
Colella, P., & Woodward, P. 1984, J. Comp. Phys., 54, 174
David, L. P., & Kempnern, J. 2004, ApJ, 613, 831
Dickey, J. M., & Lockman, F. J. 1990, ARA&A, 28, 215
Dietrich, J. P., Clowe, D. I., & Soucail, G. 2002, A&A, 394, 395
Dietrich, J. P., Schneider, P., Clowe, D., Romano-Díaz, E., & Kerp, J. 2005, A&A, 440, 453
Domainko, W., Mair, M., Kapferer, W., et al. 2006, A&A 452, 795
Durret, F., & Lima Neto, G. B. 2008, AdSpR, 42, 578
Durret, F., Gerbal, D., Lobo, C., & Pichon, C. 1999, A&A, 343, 760
Durret, F., Lima Neto, G. B., Forman, W., & Churazov, E. 2003, A&A, 403, L29
Durret, F., Lima Neto, G. B., & Forman, W. 2005, A&A, 432, 809
Durret, F., Laganá, T. F., Adami, C., & Bertin, E. 2010, A&A, 517, A94
Evrard, A. E., Bialek, J., Busha, M., et al. 2008, ApJ, 672, 122
Gunn, J., & Gott, J. 1972, ApJ, 176,1
Gwyn, S. D. J. 2009, in Astronomical Data Analysis Software and Systems XVIII, ASP Conf. Ser., 411, 123 [arXiv:0904.2568]
Hoffman, Y., & Ribak, E. 1991, ApJ, 380
Ilbert, O., Tresse, L., Zucca, E., et al. 2005, A&A, 439, 863
Kaastra, J. S., & Mewe, R. 1993, A&AS, 97, 443
Kapferer, W., Ferrari, C., Domainko, W., et al. 2006, A&A, 447, 827
Kapferer, W., Kronberger, T., Weratschnig, J., et al. 2007, A&A, 466, 813
Liedahl, D. A., Osterheld, A. L., & Goldstein, W. H. 1995, ApJ, 438, L115
Matteucci, F., & François, P. 1989, MNRAS, 239, 885
Read, A. M., & Ponman, T. J. 2003, A&A, 409, 395
Robin, A. C., Reylé, C., Derrière, S., & Picaud, S. 2003, A&A, 409, 523
Ruffert, M. 1992, A&A, 265, 82
Schindler, S., Kapferer, W., Domainko, W., et al. 2005, A&A, 435, L25
Schlegel, D. J., Finkbeiner, D. P., & Davis, M. 1998, ApJ, 500, 525
Springel, V. 2005, MNRAS, 364, 1105
Vale, A., & Ostriker, J. P. 2006, MNRAS, 371, 1179
van Kampen, E., Jimenez, R., & Peacock, J. 1999, MNRAS, 310, 43
Wright, E. L. 2006, PASP, 118, 1711